





Cite this: *Nanoscale*, 2023, **15**, 6686

Rational design of MoS₂-supported Cu single-atom catalysts by machine learning potential for enhanced peroxidase-like activity†

Deting Xu,^{a,b} Wenyan Yin, ^a Jie Zhou,^a Liyuan Wu,^a Haodong Yao,^a Minghui Sun,^a Ping Chen,^a Xiangwen Deng^a and Lina Zhao ^{*a,b}

Two-dimensional molybdenum disulfide (2D-MoS₂)-supported single atom nanomaterials with enhanced enzyme-like activities are potential substitutes for natural enzymes due to their huge specific surface areas, ease of decoration, high catalytic activity and high catalytic stability. However, their catalytic mechanism remains unclear, making the rational design of nanozymes difficult to achieve. Herein, the mechanisms have been explored to enhance the peroxidase-like activity of MoS₂ for H₂O₂ decomposition. Global neutral network (G-NN) potentials were constructed to accurately and quickly illustrate the mechanisms of MoS₂ catalysts and their surface modifications. The high peroxidase-like activity of the MoS₂-supported Cu single atom catalyst with sulfur vacancy (Cu@MoS₂-Vs) in acidic conditions was systematically evaluated using the trained G-NN potential and density functional theory (DFT), as well as experimental validation. Further analysis of the geometric and electronic properties of pivotal stationary structures revealed the enhanced electron transfer process for high catalytic performance with the modulation of the Cu single atom loading, sulfur vacancy engineering and the surrounding acidic and alkaline environment regulation on the MoS₂ basal plane. The results also showed that Cu@MoS₂-Vs in an acidic environment exhibited the highest peroxidase-like activity. This work is expected to provide broad implications for the rational design of substrate-supported single-atom catalysts with superior performance and lower cost by surface modification and acidic and alkaline environment regulation.

Received 28th December 2022,

Accepted 7th March 2023

DOI: 10.1039/d2nr07270j

rsc.li/nanoscale

1. Introduction

Nanozymes, with high stability, high catalytic activity and specified active centers, have become the frontrunners to replace natural enzymes in the future. The nanomaterials used as nanozymes mainly include metal/metal oxides, metal-organic frameworks, and carbon-based materials.¹ These nanozymes and their ramifications are expected to have great application potential in biomedical, chemical and environmental fields.^{2,3} Despite these benefits, the practical application of nanozymes still faces great challenges, particularly the rational design of nanozymes with high efficiency.

Two-dimensional (2D) materials have unique physical and chemical properties such as simple construction, controllable and multiple active sites, and large surfaces.⁴ Consequently,

2D materials are often used as potential substrates for nanozymes. Typical 2D materials include graphene,⁵ hexagonal boron nitride (h-BN),⁶ transition metal dichalcogenides (TMDs),^{7,8} graphitic carbon nitride (g-C₃N₄),⁹ and layered double hydroxides (LDHs).¹⁰ Among them, due to low cost, easy availability, commendable electronic properties, high stability and high catalytic activity, 2D molybdenum disulfide (2D-MoS₂) is widely used for the hydrogen evolution reaction (HER)¹¹ and enzymatic reaction.¹² However, studies have confirmed that the active sites of MoS₂ are mainly concentrated at edges or defect sites. The MoS₂ basal plane is catalytically inert but it occupies a large area.¹³ In order to improve the catalytic activity of the MoS₂ basal plane, various valid strategies for adding active sites have been proposed such as N-doping, surface defect engineering, and ambient microenvironment regulation.^{14–16}

Single-atom catalysts (SACs) have been an important research field in recent years. SACs have the advantages of maximum atomic utilization efficiency, high catalytic activity, flexible and adjustable electronic structures, *etc.*, which have been proved to further improve the catalytic activity after doping in 2D materials.⁸ With atomically active sites and

^aCAS Key Laboratory for Biomedical Effects of Nanomaterials and Nanosafety, Institute of High Energy Physics, Chinese Academy of Sciences, Beijing 100049, China. E-mail: linazhao@ihep.ac.cn

^bUniversity of Chinese Academy of Sciences, Beijing 100049, China

†Electronic supplementary information (ESI) available. See DOI: <https://doi.org/10.1039/d2nr07270j>



acidic conditions. We highlighted the enhanced catalytic performance of Cu@MoS₂ and anticipate that Cu@MoS₂ will provide a rational strategy for the design and development of single atom support on MoS₂ for important biomedical applications.

Merging the advantages of 2D MoS₂ and SAC catalysis, 2D MoS₂-supported SACs have been found to exhibit good performances in enzyme-like catalytic reactions and have, therefore, been widely used in electrocatalysis, photothermal tumor therapy, and nanozyme catalysis.^{18–21} There have been studies involving single-atom-based MoS₂ such as Fe-doped MoS₂ nanosheets modified with amine-polyethylene glycol (MoS₂@SA-Fe-PEG, denoted MSFP)²² and Fe@MoS₂.²³ Co-MoS₂,²⁴ single Ru atom-doped MoS₂ supported by carbon cloth (Ru-MoS₂/CC)²⁵ and Al single atom-doped MoS₂ have also been studied for enhancing the enzymatic activity of MoS₂.²⁶ As a cheap and readily available material, non-noble Cu is also expected to be applied in 2D MoS₂ supported SACs. A 2D MoS₂-supported Cu single atom catalyst, denoted as Cu@MoS₂, has been successfully synthesized and applied as a high-performance electrocatalyst for overall water splitting by altering the surface charge distribution and electronic band structure,²⁷ in efficient hydrogen evolution due to changes in atomic coordination structures,²⁸ and in low-temperature CO oxidation due to the charge transfer between the SAC and the substrate.²⁹ Like other 2D MoS₂-supported nanomaterials, Cu@MoS₂ is also expected to exhibit enzyme-like catalytic activity for biomedical applications, but its actual catalytic mechanism is still unclear, which makes the rational design an obstacle.

Theoretical and experimental studies were systematically implemented to explore the peroxidase-like activity of MoS₂ and its ramifications by rational design. To gain insight into the mechanisms that govern the activity and selectivity of MoS₂ catalysts, it is important to clarify the detailed reaction paths and electronic properties of pivotal stationary structures. DFT methods have played a significant role in optimizing the reaction paths and improving the catalytic activity at the atomic electron level in the past decade.^{30,31} In this regard, we systematically studied the reaction mechanism and rational design of 2D-MoS₂. We constructed 2D-MoS₂, MoS₂-supported Cu single atom catalyst (Cu@MoS₂), and MoS₂-supported Cu single atom catalyst with sulfur vacancy (Cu@MoS₂-Vs) and systematically explored their enzyme-like performances on the catalytic decomposition of H₂O₂ under different acidic and basic conditions using the global neutral network (G-NN) potential and stochastic surface walking (SSW) method. Through Cu single atom loading, sulfur vacancy engineering and acidic and alkaline microenvironment regulation, the rational design of 2D MoS₂ was implemented and investigated to greatly enhance the peroxidase-like catalytic activity. Electronic structure properties were analyzed to illustrate the greatly improved peroxidase-like activity of Cu@MoS₂. Furthermore, through kinetic experiments, we confirmed the enhanced performance of Cu@MoS₂ with sulfur vacancy in

2. Computational and experimental details

2.1 SSW-NN simulation

As performed in the LASP (Large-scale Atomistic Simulation with neural network Potential) code,³² the stochastic surface walking (SSW) global optimization in combination with the neural network (NN) (SSW-NN) method was applied to build global NN potential for the Cu@MoS₂ system.³³ The SSW method uses an unbiased universal potential energy surface (PES) searching method to search for the global minima (GM) structure by smoothly manipulating the structural configuration from one minimum to another on the PES.³⁴ The machine learning NN potential was generated by iterative self-learning of the plane-wave density functional theory (DFT) global PES data set generated from SSW exploration.³⁵ The process of SSW-NN is as follows: global data set generated by SSW simulation, NN potential fitting and global optimization utilizing NN potential and, finally, the convergence standard of the training reached 6.5 meV per atom for the energy and 0.212 eV Å⁻¹ for the force, which is accurate enough for the simulation of the system. The double-ended surface walking (DESW) method was implemented to locate the transition state (TS) and build the most favorable pathway between the reactants and products using only the first derivatives.

2.2 DFT calculations

Electronic structure calculations were performed using the Vienna *Ab initio* Simulation Package (VASP) with considerable precision.³⁶ All structures are relaxed within the generalized gradient approximation (GGA) method.³⁷ As for the mutual effect, we mainly calculated the Perdew–Burke–Ernzerhof (PBE) exchange–correlation functionals,³⁸ and van der Waals interactions were also considered to add a correction to the DFT-D3 method.³⁹ All calculations include spin polarization. A cutoff energy of 500 eV was employed, accompanied by a plane-wave basis set in all systems. In our calculations, a $4 \times 4 \times 1$ MoS₂ supercell was built as an initial pure configuration that is large enough for calculating the peroxidase-like processes. During structural optimization processes, a $2 \times 2 \times 1$ k -point grid was set as the Brillouin-zone integration, and a $5 \times 5 \times 1$ k -point grid was used for electronic structural calculations. A 15 Å vacuum space along the z-direction was set for avoiding layer-to-layer interactions. We ended the simulation at 0.01 eV Å⁻¹ for the force convergence criterion, and the total energy convergence threshold reached 10^{-6} eV. The calculation of adsorption energy E_{ads} (eV) was as follows:

$$E_{\text{ads}} = E_{\text{slab-molecule}} - E_{\text{molecule}} - E_{\text{slab}} \quad (1)$$

where $E_{\text{slab-molecule}}$ is the total energy of the optimized system, E_{molecule} is the energy of an adsorbed molecule in the isolated state, and E_{slab} is the energy of the slab.

2.3 Synthesis of Cu@MoS₂ nanozymes

MoS₂ nanozymes with the morphology of nanosheets were synthesized by a simple hydrothermal method according to our previous report.⁴⁰ Then, to obtain Cu ions-loaded Cu@MoS₂ nanozymes, 10 mL (10 mg mL⁻¹) of the obtained MoS₂ nanosheets aqueous solution was mixed with 10 mg of powder CuCl₂·2H₂O under sonication for 10 min based on the electrostatic interaction of negatively charged MoS₂ nanosheets and the positively charged Cu ions. Finally, the as-obtained Cu@MoS₂ nanozymes were washed with distilled water three times *via* centrifugation. The loading ratio of Cu single atoms in MoS₂ was 5.02%, calculated by inductively coupled plasma mass spectrometry (ICP-MS).

2.4 Peroxidase-like activity and kinetic assay

The MoS₂ and Cu@MoS₂ can catalyze the oxidation of the colorless 3,3',5,5'-tetramethylbenzidine (TMB) to form the blue oxidized TMB (oxTMB) with the maximum absorption peak at 652 nm in the presence of the electron acceptor H₂O₂. Typically, the pH-dependent peroxidase-like activity of MoS₂ and Cu@MoS₂ containing H₂O₂ (1 mM) and TMB (1 mM) in phosphate-buffered saline (PBS) buffer with different pH values (4.0, 5.5, 6.0, 7.4, 8.0) was explored and compared at 37 °C.

The peroxidase-like activities of MoS₂ (20 μg mL⁻¹) and Cu@MoS₂ (20 μg mL⁻¹) were respectively tested in PBS buffer (pH 4.5, adjusted by HCl) containing different concentrations of H₂O₂ and TMB as substrates. The microplate reader (SpectraMax M2MDC) was used to measure the UV-vis absorbance of the blue oxTMB at a set time point after varying the

concentrations of the H₂O₂ substrate *versus* another TMB substrate at 37 °C. According to the Michaelis–Menten eqn (2), the Lineweaver–Burk double-reciprocal plot of eqn (3), and the initial reaction rates (V_0) calculated from the absorbance changes during the varied H₂O₂ or TMB concentration, kinetic parameters including Michaelis constant (K_m) and the maximal reaction velocity (V_{max}) can be obtained by a linear-fitting method. The V_{max} is obtained when the nanozymes are saturated with the substrate and $[S]$ is the concentration of the substrate.

$$\nu_0 = \frac{V_{\text{max}} \cdot [S]}{V_{\text{max}} + [S]} \quad (2)$$

$$\frac{1}{\nu_0} = \frac{K_m}{V_{\text{max}}} \cdot \frac{1}{[S]} + \frac{1}{V_{\text{max}}} \quad (3)$$

3. Results and discussion

3.1 Enzyme-like properties of pristine MoS₂

To explore the effects of the surface rational design with Cu single atom loading, sulfur vacancy engineering and acidic and alkaline environment regulation on the peroxidase-like activity of MoS₂, we constructed a series of catalyst structures based on the pure monolayer MoS₂ surface (Fig. 1 and S1†).

As a 2D support substrate, MoS₂ exhibits the potential for catalytic activities. On this basis, we systematically studied the enzyme-like activities of pure MoS₂. The optimized initial configuration of the pure MoS₂ surface is shown in Fig. 1. The average distance between three adjacent S atoms of MoS₂ was 3.231 Å (Table S1†). Using the SSW method, we obtained a series of possible stable adsorption structures after H₂O₂ decomposition, including H₂O₂*, HO*, HOO*, H₂O*, O* and proton species. Subsequently, the DESW method was used to

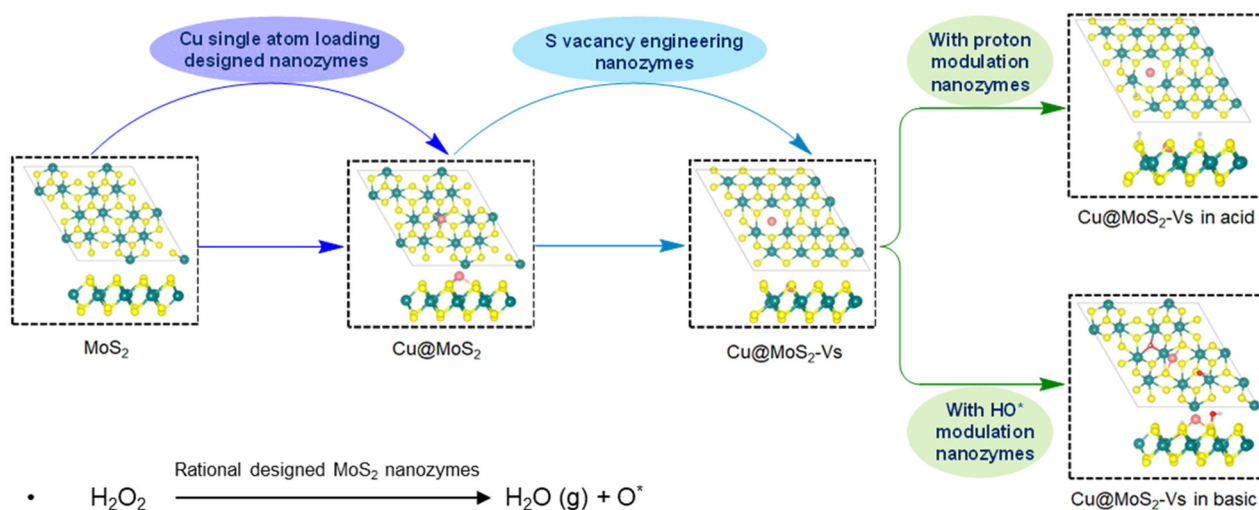


Fig. 1 A schematic diagram of the rational design of MoS₂ nanozymes to modulate peroxidase-like activity through surface modification with Cu single atom loading, sulfur vacancy and acidic and alkaline environment regulation. The spheres in green, yellow, pink, red and gray represent Mo, S, Cu, O and H atoms, respectively.



connect the reactants with the products to find transition states and the reaction paths. Firstly, H_2O_2 was adsorbed parallel to the substrate with a low adsorption energy of -0.31 eV (Table S2†). There was negligible electron aggregation between the H_2O_2 molecule and MoS_2 after H_2O_2 adsorption, suggesting weak interaction between the H_2O_2 molecule and substrate (Fig. S2a†). H_2O_2 has two possible decomposition pathways on the pure MoS_2 surface. One possible pathway is as shown in Fig. S3,† where H_2O_2 possibly decomposed into HOO^* and H^* species that needed to overcome a high energy barrier of 3.00 eV . On the other hand, the O–O bond of H_2O_2 will be elongated to form two HO^* species, overcoming an energy barrier of 1.81 eV , which is the rate-determining step of the whole reaction path. One HO^* species was transferred to an adjacent sulfur atom with an energy barrier of 1.26 eV (Fig. 2).

On comparing these two reaction pathways, we concluded that the H_2O_2 decomposition into two HO^* species needs a smaller energy barrier, which means that MoS_2 prefers to demonstrate peroxidase-like activity with HO^* species generation. However, the peroxidase-like activity of pure MoS_2 is chemically inert at the basal plane and needs relatively higher energy to be activated. Various rational design strategies are urgently needed to improve the peroxidase-like activity to achieve better practical applications. Therefore, a series of

modifications were proposed to improve the peroxidase-like performance of MoS_2 , including surface modification with Cu single atom loading, sulfur vacancy engineering and acidic and alkaline microenvironment regulation.

3.2 Peroxidase-like activity of Cu@MoS_2

The loading of the Cu single atom on the MoS_2 support can change the electronic structure and improve its peroxidase-like activity. We randomly placed a Cu single atom above a pure MoS_2 support, and the SSW method was used to globally optimize all possible adsorption sites of the Cu single atom. Ultimately, we obtained the most stable MoS_2 -supported Cu adsorption structure (denoted as Cu@MoS_2) (Fig. 1). The Cu single atom was stably adsorbed at the hollow site above the Mo atom. As Cu was adsorbed, the average distance between the three S atoms neighbouring the Cu single atom became 3.346 \AA on Cu@MoS_2 , which was 0.115 \AA longer than that of MoS_2 (Table S1†). The extended distance makes it easier for the Cu single atom to attach to the slab. Simulation results showed that the adsorption energy of the Cu single atom on the MoS_2 support was -3.27 eV , which indicated that the Cu single atom was stably adsorbed on Cu@MoS_2 (Table S3†). Bader charge analysis was implemented to further elucidate the effects of the Cu single atom loading on the peroxidase-like activity of MoS_2 (Table S4†). The charge density difference plots are shown in Fig. S4,† where the cyan and purple regions correspond to electron accumulation and depletion, respectively. Accordingly, it can be seen from the charge density difference results that there was some electron depletion on the adsorbed Cu single atom and Mo atoms. The electron accumulation between the interacting Cu single atom and three sulfur atoms significantly indicates the covalent interaction between the adsorbed Cu single atom and the MoS_2 support (Fig. S4b†). The accumulation of the electron density suggests the chemical bonds formation of Cu–S bonds, which indicates that the Cu atom was chemically adsorbed on the MoS_2 support. The strong interaction between Cu and the MoS_2 support was also verified by the Bader charge results, where the electrons transferred from Cu to adjust S atoms with a value of $-0.53|e|$. The electronic property results showed that the Cu@MoS_2 structure is stable, suggesting that a Cu single atom can provide a stable active site for H_2O_2 decomposition.

Furthermore, we systematically studied the peroxidase-like activity of Cu@MoS_2 catalysing the decomposition of the H_2O_2 substrate. As shown in Fig. 2, on the Cu@MoS_2 surface, H_2O_2 was firstly chemically adsorbed on the Cu active site with an adsorption energy of -0.80 eV (Table S2†). As shown in Fig. S5,† we denoted the O atom of the H_2O_2 molecule that directly interacted with the catalyst surface as $\text{O1}'$, and the corresponding H atom of H_2O_2 that bonded with $\text{O1}'$ was denoted as $\text{H1}'$. The other O atom and H atom were respectively denoted as $\text{O2}'$ and $\text{H2}'$. After H_2O_2 adsorption, some electrons were localized mainly between the surface Cu atom and $\text{O1}'$, while there were few electrons at $\text{O1}'$ on Cu@MoS_2 , which was in line with the Bader charge results in Table 1, indicating the obvious overlap between the H_2O_2 molecule and

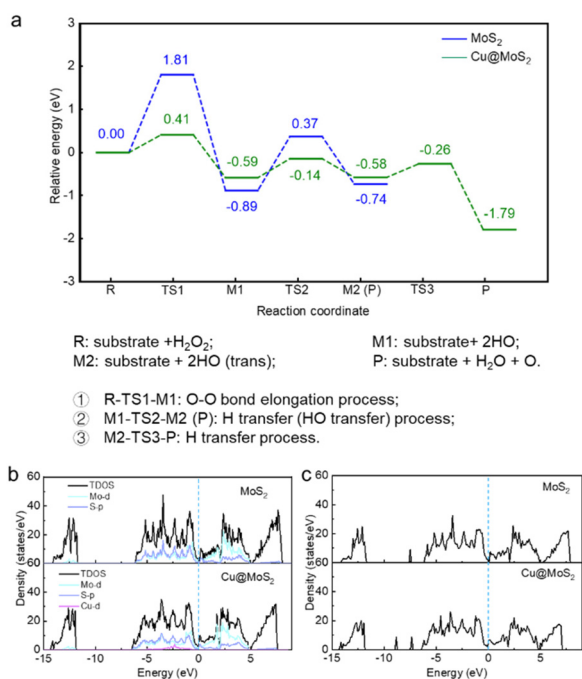


Fig. 2 (a) Energy profile for the decomposition of H_2O_2 on pure MoS_2 and Cu@MoS_2 surfaces. The blue and green curves show the decomposition process of H_2O_2 on the surface of pure MoS_2 and Cu@MoS_2 catalysts, respectively. The numbers represent the energy (eV) at each state. The abscissa R, TS, M1, and P represent reactants, transition states, intermediates, and products, respectively. (b) TDOS and PDOS of MoS_2 and Cu@MoS_2 substrates. (c) TDOS of H_2O_2 adsorption on MoS_2 and Cu@MoS_2 substrates.



Table 1 Bader charge analysis of pure MoS₂, Cu@MoS₂, Cu@MoS₂-Vs, and Cu@MoS₂-Vs in acidic and basic conditions before and after H₂O₂ adsorption. A positive value means that the atom gained electrons, whereas a negative value means that the atom lost electrons

	Pure MoS ₂		Cu@MoS ₂ -Vs		Cu@MoS ₂ -Vs in acid		Cu@MoS ₂ -Vs in basic	
	Before ads	Ads	Before ads	Ads	Before ads	Ads	Before ads	Ads
Mo (S) average	0.54	0.55	−0.99	−0.98	−1.00	−0.99	−1.17	−1.17
Mo	−1.07	−1.07	—	—	—	—	—	—
Cu	—	—	−0.08	−0.17	−0.02	−0.24	−0.48	−0.60
O1'	—	0.62	—	0.64	—	0.69	—	0.64
O2'	—	0.63	—	0.57	—	0.60	—	0.59
H1'	—	−0.61	—	−0.62	—	−0.65	—	−0.62
H2'	—	−0.62	—	−0.60	—	−0.63	—	−0.65

the Cu single atom (Fig. S2b†). The O–O bond of H₂O₂ stretched to 1.498 Å, which was longer than that in the gas phase, indicating H₂O₂ activation. The elongation of the bond length was mostly attributed to the electron transfer from the primary bond to the newly formed bond between the H₂O₂ molecule and substrate. Further, H₂O₂ decomposed into H₂O molecules and O* species after three processes of O–O bond stretching, hydroxyl migration and H transfer, which only overcame low barriers of 0.41, 0.45 and 0.32 eV, respectively, and with a high exothermic energy of 1.79 eV. It was revealed that Cu single atom loading greatly reduced the energy barrier required for the rate-determining step, resulting in enhanced reactive activation. The energy required for H₂O₂ decomposition on Cu@MoS₂ was 1.40 eV lower than that required for the pure MoS₂ surface, suggesting that Cu single atom adsorption enhanced the peroxidase-like catalytic activity of Cu@MoS₂.

To gain more insight into the electronic behaviour of MoS₂ with or without Cu single atom loading systems, we calculated the total density of states (TDOS) as well as the projected density of states (PDOS) as shown in Fig. 2b. Compared with that of pure MoS₂, the electron distribution of the Cu@MoS₂ around the Fermi level (E_f) slightly increased, which indicated that the loading of the Cu single atom enhanced the metallic property of MoS₂. In addition, the TDOS of Cu@MoS₂ shifted to the left, suggesting that loading the Cu single atom increased the electrons of the MoS₂ system. As a result, the Cu single atom became the active site for Cu@MoS₂ to catalyse the H₂O₂ decomposition. It can be seen from the PDOS result that Cu-d orbital and S-p orbital are strongly hybridized, indicating that the Cu atom was stably adsorbed on the MoS₂ substrate. Also, we studied the DOS with respect to the E_f of H₂O₂ adsorption on MoS₂ and Cu@MoS₂ (Fig. 2c). We found that the electron energy state of H₂O₂ adsorbed on the Cu@MoS₂ substrate was much lower than that on MoS₂, indicating that the electron transfer was more likely to occur when H₂O₂ was adsorbed on Cu@MoS₂. In summary, DOS analysis results showed that Cu@MoS₂ can provide more electrons for H₂O₂ to promote O–O bond breaking, further enhancing the peroxidase-like catalytic activity.

3.3 The enhanced peroxidase-like performance of Cu@MoS₂-Vs

The design of sulfur vacancy engineering has been widely reported to regulate the intrinsic electronic properties and

induce local electronic environment redistribution, thus greatly enhancing their catalytic performance. To study the sulfur vacancy engineering effects, a sulfur atom was randomly removed from the pure MoS₂ surface, and a stable configuration was obtained after SSW global optimization (Fig. S1a†). We added the Cu single atom to obtain the stable Cu@MoS₂-Vs structure using the SSW method (Fig. 1). Unlike the Cu@MoS₂ surface, the Cu single atom was more inclined to fill and adsorb at the S vacancy site with Cu@MoS₂-Vs. The adsorption energy of the Cu single atom on the surface Cu@MoS₂-Vs was −4.96 eV, indicating that the Cu single atom was stably adsorbed on Cu@MoS₂-Vs. In addition, the adsorption energy was more negative than that of Cu@MoS₂ with the value of −3.27 eV, indicating that the Cu single atom active site was more stable when bonded to the Cu@MoS₂-Vs catalyst. Subsequently, Bader charge and charge density difference analysis were simultaneously carried out on the Cu@MoS₂-Vs surface to clarify the effects of the sulfur vacancy on the peroxidase-like activity of Cu@MoS₂ (Fig. S4, and Table S1†). We recorded the charge transfer between adjacent S, Mo atoms and the Cu single atom of the Cu@MoS₂-Vs surface. As for Cu@MoS₂-Vs, the three Mo atoms of the slab around Cu respectively transferred 0.99, 0.99 and 1.00|e|, and the Cu atom also lost some electrons correspondingly. Also, there was electron depletion on the adsorbed Cu atom and three Mo atoms on the Cu@MoS₂-Vs surface. The electrons increased between Cu and Mo atoms, which suggested the strong metal–support interaction after the adsorption of the Cu atom (Fig. S4c†). Accordingly, it can be seen from the charge density difference results that there was great overlapping of the charge density on Cu@MoS₂-Vs, indicating a strong coupling between Cu and the slab (Fig. S4c†). It was also shown that there was a covalent bond for electrons converging between the Cu single atom and the support. The geometric and electronic structure analysis of the surface Cu@MoS₂-Vs showed that the sulfur vacancy promoted the adsorption of the Cu single atom on MoS₂.

The reaction pathway was calculated to explore the function of sulfur vacancy engineering in the enhanced intrinsic peroxidase-like activity of Cu@MoS₂-Vs. Using the stable configurations of the reactant, product and intermediates obtained by the SSW method, we applied the DESW method to establish all possible reaction paths and their chemical bond-making/





Fig. 3 (a) Schematic diagram of the H_2O_2 decomposition reaction cycle on $\text{Cu@MoS}_2\text{-Vs}$. (b) Energy profiles of $\text{Cu@MoS}_2\text{-Vs}$ in neutral, acidic and alkaline conditions. The numbers represent the energy (eV) at each state. The abscissa TS, M, and P represent transition states, intermediates and products, respectively.

breaking transition states (TS) of H_2O_2 decomposition on the $\text{Cu@MoS}_2\text{-Vs}$ surface to study its peroxidase-like catalytic performance. In Fig. 3a, the catalytic cycle on the catalyst surface generally includes four stages: H_2O_2 adsorption, O–O bond stretching, H transfer and TMB substrate oxidation. As shown in Fig. 3b, with $\text{Cu@MoS}_2\text{-Vs}$ (energy profile in green line), H_2O_2 was adsorbed with the highest adsorption energy of -0.89 eV, which was due to chemisorption. It was confirmed by visualizing the charge density difference that a chemical bond was formed between H_2O_2 and the Cu single atom. In addition, H_2' had an electron coupling with the surface sulfur atom. The interaction between $\text{H}_2'\text{-S}$ and $\text{O}1'\text{-Cu}$ jointly led to stronger adsorption and further activation of H_2O_2 (Fig. 3b). The $\text{O}1'\text{-O}2'$ bond length was elongated to 1.472 Å. The H_2O_2 molecule went through a transition state to decompose into two HO^* species, which was the rate-determining step of the whole reaction and required overcoming a barrier of 0.51 eV. The subsequent H transfer process was accompanied by a nearly zero energy barrier (0.05 eV). The entire reaction process was thermodynamically favourable with a large exothermic energy of 4.13 eV. The results showed that the loading of the Cu single atom greatly reduced the energy barrier of the rate-determining step, and the sulfur vacancy was beneficial for system exothermicity. The decomposition of H_2O_2 into two HO^* species on $\text{Cu@MoS}_2\text{-Vs}$ was both kinetically and thermodynamically favourable, which indicated that the $\text{Cu@MoS}_2\text{-Vs}$ was the most ideal peroxidase-like nanozyme as compared with pure MoS_2 and Cu@MoS_2 .

3.4 The acidic and alkaline environment regulation of the peroxidase-like properties of $\text{Cu@MoS}_2\text{-Vs}$

To better simulate the peroxidase-like activity of $\text{Cu@MoS}_2\text{-Vs}$ in real physiological conditions, we investigated the effects of acidity and alkaline conditions on $\text{Cu@MoS}_2\text{-Vs}$.

The pre-adsorbed OH and H^* groups on $\text{Cu@MoS}_2\text{-Vs}$ surfaces can only be advantageously developed in basic and acidic environments, respectively, which can lead to acidic and alkaline environment regulation and POD-like activities.⁴¹ Therefore, two protons and two hydroxyl groups were ran-

domly added to $\text{Cu@MoS}_2\text{-Vs}$ to simulate acidic and alkaline environments, respectively. Firstly, stable catalyst configurations were obtained by the SSW global optimization of $\text{Cu@MoS}_2\text{-Vs}$ in neutral, acidic and basic conditions (Fig. 1). The neutral conditions have been discussed above regarding the structure and catalytic performance of $\text{Cu@MoS}_2\text{-Vs}$ (section 3.3). In acidic conditions, two protons were respectively adsorbed on sulfur atoms near the active site with H–S bond lengths of 1.362 Å. The Cu atom was stably adsorbed at the sulfur vacancy site. The average distance between the three neighbouring sulfur atoms was 0.053 Å longer than that under neutral conditions and the average distance between the three Mo atoms was 0.070 Å longer than that under neutral conditions. The elongated distance caused the steadier adsorption of the Cu single atom on $\text{Cu@MoS}_2\text{-Vs}$. In basic conditions, one of the two HO^* radicals preferred to adsorb at the sulfur vacancy. Another HO^* radical preferred to adsorb on sulfur atoms. In addition, the adsorption energies of the Cu single atom were -3.74 and -2.79 eV in acidic and basic conditions, respectively, suggesting the stable adsorption of the Cu single atom in both acidic and basic conditions.

The H_2O_2 adsorption and decomposition abilities of $\text{Cu@MoS}_2\text{-Vs}$ under different acidic and alkaline environments were analysed through the energy profile. H_2O_2 was added to the surface to obtain stable adsorption configurations in different acidic and alkaline microenvironments. The energy profiles of the most favourable route for the H_2O_2 decomposition in acid and basic conditions are shown in Fig. 3b. Under acidic conditions, H_2O_2 was adsorbed steadily and obliquely on Cu single atom active sites with an adsorption energy of -0.83 eV. Then, only a 0.24 eV barrier was needed to be overcome to form two HO^* groups. These HO^* groups quickly combined with the H on the surface to form two H_2O molecules. The entire reaction process was thermally favourable with a large exothermic energy of 6.65 eV. However, in an alkaline environment, H_2O_2 was chemically adsorbed on Cu single atom active sites with an adsorption energy of -1.03 eV. H_2O_2 decomposition needed to overcome an energy barrier of 0.92 eV to break the O–O bond. Subsequently, the two HO^* groups



were adsorbed on the Cu single atom and underwent two H transfer processes to form two H₂O molecules and two O* species, requiring energy barriers of 1.37 and 0.06 eV, respectively. The formation of the first H₂O molecule became the rate-determining step, which required overcoming larger obstacles. From the perspective of the reaction paths, the alkaline conditions are not conducive to the decomposition of H₂O₂ on the surface of Cu@MoS₂-Vs as compared with the neutral environment. On the contrary, acidic environments not only greatly reduced the reaction energy barrier of H₂O₂ decomposition, but also caused the reaction to release the most heat.

3.5 The accelerated electron transfer process: the essence of high peroxidase-like performance

The low energy barrier of the rate-determining step directly reflects high catalytic activity, and the essence of the low energy barrier is reflected in the basic electronic and structural properties. The electronic structural properties were further analysed to elucidate the intrinsic origin of the high peroxidase-like activity and high-activity sites of the kinetically and thermodynamically favourable Cu@MoS₂-Vs catalyst under acidic conditions.

After H₂O₂ was adsorbed on the Cu@MoS₂-Vs catalyst surface in neutral, acidic and basic conditions, the charge density difference diagram showed that there were electron transfers between the H₂O₂ molecule and catalysts to different degrees (Fig. 4a–c). The Cu single atoms of catalysts all had obvious bond interactions with H₂O₂. As shown in Table 1, Cu atoms on Cu@MoS₂-Vs catalysts have different degrees of electron transfer in different acidic and alkaline environments.

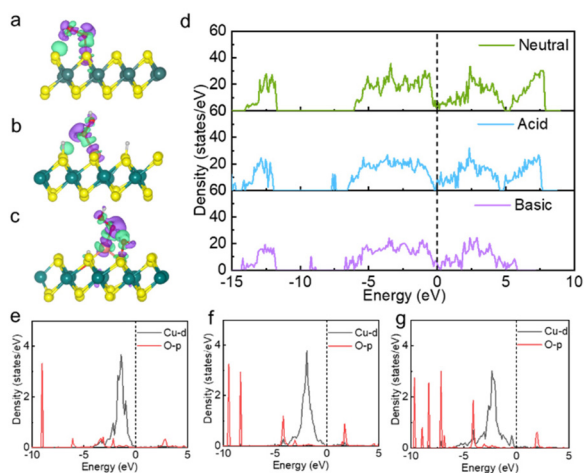


Fig. 4 Charge density difference for H₂O₂ adsorption on Cu@MoS₂-Vs in (a) neutral, (b) acidic and (c) basic conditions, respectively. The isosurface value of electron density was taken as 0.002 e Å⁻³. The cyan and purple regions for the charge density difference represent the areas of electron accumulation and depletion, respectively. (d) TDOS of Cu@MoS₂-Vs in different conditions of acidity and alkalinity. (e and f) PDOS of Cu-d and O-p orbitals of Cu@MoS₂-Vs in (e) neutral, (f) acidic and (g) alkaline conditions.

Under neutral conditions, the Cu atom adsorbed by the H₂O₂ molecule loses 0.09 electrons, while in an acidic environment, the Cu atom loses 0.22 electrons, which is 0.13 electrons more than in neutral conditions. Under basic conditions, the Cu atom loses 0.12 electrons. The O1' atoms in different acid and alkaline environments all gained more electrons (0.64|e| in neutral and basic conditions, 0.69|e| in acidic conditions) as compared to pure MoS₂ (0.62|e|). The O1' atom gained the most electrons in acidic conditions. These results indicated that Cu single atom loading, sulfur vacancy engineering and the acidic and alkaline environment regulation can modulate the degree of electron transfer between adsorbed H₂O₂ molecules and catalyst surfaces. More importantly, acidic conditions can promote better electron transfer between H₂O₂ and the support as compared to neutral and basic conditions.

TDOS and projected density of states (PDOS) were performed to further confirm the binding nature as well as the electronic properties of the considered systems. TDOS of Cu@MoS₂-Vs substrates under different acidic and alkaline environments are shown in Fig. 4d. Under acidic conditions, there was a left shift of TDOS, indicating the increased electron properties of Cu@MoS₂-Vs. Meanwhile, new peaks at −7.5 eV, and −14.8 eV were added at the valence band. In addition, the electronic state at the E_f increased, which indicated that the acidic condition increased the electrical conductivity of the catalyst. Further PDOS analysis revealed that electrical conductivity mainly resulted from the overlapping of Mo-d, S-p, and Cu-d orbitals (Fig. S6†). DOS results showed that the acid environment is conducive to the subsequent electron transfer between the H₂O₂ molecule and the substrates. However, the electronic density decreased on Cu@MoS₂-Vs in basic conditions. The electron state density near 6.0 eV to 7.5 eV on the conduction band side disappeared and new peaks appeared at −6.7 eV, −8.9 eV and −9.2 eV on the valence band side. Cu-d and O-p orbitals were to varying degrees overlapped in neutral, acidic and alkaline environments. H₂O₂ molecules bonded more strongly with Cu single atom on the surface under basic conditions than neutral or acidic conditions (Fig. 4e and f).

We also analysed the relationship between the activity for H₂O₂ decomposition and the adsorption energy of H₂O₂ molecules on a range of MoS₂-based surfaces. The results showed that the H₂O₂ dissociation was well in line with the volcano plot (Fig. S7†).⁴² The Cu single atom loading, sulfur defect engineering and the adjustment of the acid and alkaline environment caused the adsorption capacity of MoS₂ to increase, and thus the catalytic activity increased accordingly. The too-small adsorption energy of H₂O₂ on the surface of pure MoS₂ or the too-large adsorption energy on Cu@MoS₂-Vs in alkaline environments is not conducive to catalytic activity. The acidic environment causes the Cu@MoS₂-Vs surface to have the optimal adsorption energy, which led to the best catalytic efficiency.

The analysis of the geometric structure and electronic structure showed that the loading of Cu single atoms, sulfur defect engineering and regulation of acidic conditions led to the optimal adsorption energy of the H₂O₂ molecule, accelerated





Fig. 5 (a) Relative catalytic activity of the MoS₂ and Cu@MoS₂ as peroxidase mimics under different pH values at 37 °C tested by UV-vis absorption of oxTMB. The velocity of the reaction between [•]OH and the various concentrations of H₂O₂ in the presence of (b) MoS₂ and (c) Cu@MoS₂. The successful Cu loading on the MoS₂ surface was well in agreement with the DFT calculations.

the electron transfer rate, and therefore greatly promoted the peroxidase-like enzymic activity.

3.6 Kinetic experiments on the peroxidase-like properties of MoS₂ and Cu@MoS₂ with sulfur vacancy in acid conditions

To experimentally verify the pH-dependent peroxidase-like catalytic activities of the as-synthesized MoS₂ and Cu@MoS₂ nanosheets, we performed the catalytic oxidation of the chromogenic substrate of the colorless 3,3',5,5'-tetramethylbenzidine (TMB) in the presence of H₂O₂ at 37 °C (Fig. 5a). The default 0 K setting during the theoretical calculation was due to the limitations of the potential functional training methods (SSW and DESW) in LASP, but it did not affect the consistency of the theoretical and experimental results after free energy correction (Table S2†). The UV-vis absorption of the blue oxidized TMB (oxTMB) showed that both the MoS₂ and Cu@MoS₂ nanosheets had high peroxidase-like catalytic activities at pH 4.0 due to the easy generation of [•]OH. Particularly, the Cu@MoS₂ nanosheets had a relatively higher peroxidase-like catalytic activity than the MoS₂ nanosheets at pH 4.0. With the pH value changing from 5.0 to 8.0, both the MoS₂ and Cu@MoS₂ nanosheets suffered from reduced catalytic activity. However, the maintained value of the catalytic activity of Cu@MoS₂ nanosheets was significantly higher than that of the MoS₂ nanosheets.

The Michaelis-Menten kinetic graphs of MoS₂ and Cu@MoS₂ nanosheets were obtained using the initial rate *versus* the concentrations of H₂O₂ at pH 4.5 (Fig. 5b and c). The steady-state kinetics of MoS₂ and Cu@MoS₂ nanosheets matched well with the typical Michaelis-Menten steady-state kinetics model in various concentration ranges of H₂O₂. In Table 2, the lower Michaelis-Menten constant (*K_m*) of the Cu@MoS₂ nanosheets was 2.05 mmol L⁻¹, suggesting the

higher binding affinity of the Cu@MoS₂ nanosheets for the H₂O₂ substrate as compared to the MoS₂. Also, the maximum velocity (*V_{max}*) of Cu@MoS₂ nanosheets was calculated to be 1.09 × 10⁻⁷ mmol L⁻¹ s⁻¹, which was significantly higher than that of the MoS₂ nanosheets. These results suggest that the H₂O₂ concentration-dependent oxidation kinetics of Cu@MoS₂ can promote the enhancement of the peroxidase-like catalytic activity of the MoS₂ in acidic conditions because of the successful Cu loading on the MoS₂ surface, which was well in agreement with the DFT calculations.

4. Conclusions

The rational design and regulation of single-atom loaded MoS₂ nanozymes are the key drawbacks to be overcome for use as substitutes for natural enzymes. Through neural network potential trained by machine learning, the potential including Mo, S, Cu, O, and H elements was successfully constructed and was used to search the stable configurations and their transition states rapidly and massively to efficiently find the reaction path of H₂O₂ decomposition on different catalyst surfaces. The simulation results showed that the activity of the peroxidase-like nanozyme of MoS₂ was increased by Cu single atom loading. In particular, the peroxidase-like activity of Cu@MoS₂ modified with sulfur vacancy was greatly increased under acidic conditions. The electronic properties calculations further confirmed that the Cu single-atom loading and sulfur vacancy effect, and acidic and alkaline microenvironment regulation affected the electron transfer process of catalysts by changing their electronic properties. The results showed that Cu@MoS₂-Vs under acidic conditions accelerated the electron transfer process, thus further promoting the activation of adsorbed H₂O₂ molecules and enhancing the peroxidase-like activity. At the same time, acidic and alkaline environments affect the density of states of the catalysts. The alkaline environment reduces the density of states of Cu@MoS₂-Vs, thus limiting the electron transfer process to some extent and inhibiting the decomposition of H₂O₂. Furthermore, kinetics experiments demonstrated that the peroxidase-like activity was greatly improved by Cu loading and the adjustment of the

Table 2 Comparison of the kinetics based on the peroxidase-like activity of the MoS₂ nanozyme and Cu@MoS₂ nanozyme

Catalyst	Substrate	<i>K_m</i> (mmol L ⁻¹)	<i>V_{max}</i> (mmol L ⁻¹ s ⁻¹)
MoS ₂	H ₂ O ₂	4.94	0.54 × 10 ⁻⁷
Cu@MoS ₂	H ₂ O ₂	2.05	1.09 × 10 ⁻⁷



acidic and alkaline environments. Our results show that surface modification with Cu single atom loading, sulfur vacancy engineering and acidic and alkaline environment regulation can significantly improve the peroxidase-like activity of MoS₂ theoretically and experimentally, which provides guidance for the rational design of nanozymes in the future, and is expected to be applied in the free radical generation and scavenging.

Author contributions

The manuscript was written through contributions of all authors. All authors have given approval to the final version of the manuscript.

Conflicts of interest

There are no conflicts to declare.

Acknowledgements

The work was supported by the National Key Research and Development Program of China (2021YFA1200904 and 2020YFA0710700), the National Natural Science Foundation of China (31971311, 62205338), the Innovation Program for IHEP (E35457U210), Xie Jialin Foundation of IHEP (E2546EU210).

References

- 1 Z. R. Wang, R. F. Zhang, X. Y. Yan and K. L. Fan, *Mater. Today*, 2020, **41**, 81–119.
- 2 Y. Y. Huang, J. S. Ren and X. G. Qu, *Chem. Rev.*, 2019, **119**, 4357–4412.
- 3 J. J. X. Wu, X. Y. Wang, Q. Wang, Z. P. Lou, S. R. Li, Y. Y. Zhu, L. Qin and H. Wei, *Chem. Soc. Rev.*, 2019, **48**, 1004–1076.
- 4 C. L. Tan, X. H. Cao, X. J. Wu, Q. Y. He, J. Yang, X. Zhang, J. Z. Chen, W. Zhao, S. K. Han, G. H. Nam, M. Sindoro and H. Zhang, *Chem. Rev.*, 2017, **117**, 6225–6331.
- 5 K. S. Novoselov, A. K. Geim, S. V. Morozov, D. Jiang, Y. Zhang, S. V. Dubonos, I. V. Grigorieva and A. A. Firsov, *Science*, 2004, **306**, 666–669.
- 6 Q. H. Weng, X. B. Wang, X. Wang, Y. Bando and D. Golberg, *Chem. Soc. Rev.*, 2016, **45**, 3989–4012.
- 7 K. L. Tan and B. H. Hameed, *J. Taiwan Inst. Chem. Eng.*, 2017, **74**, 25–48.
- 8 X. Wang, Y. W. Zhang, J. Wu, Z. Zhang, Q. L. Liao, Z. Kang and Y. Zhang, *Chem. Rev.*, 2022, **122**, 1273–1348.
- 9 C. Y. Zhi, Y. Bando, C. C. Tang, H. Kuwahara and D. Golberg, *Adv. Mater.*, 2009, **21**, 2889–2893.
- 10 Q. Wang and D. O'Hare, *Chem. Rev.*, 2012, **112**, 4124–4155.
- 11 S. W. Niu, J. Y. Cai and G. M. Wang, *Nano Res.*, 2021, **14**, 1985–2002.
- 12 X. Li and H. Zhu, *J. Materiomics*, 2015, **1**, 33–44.
- 13 S. Y. Cho, S. J. Kim, Y. Lee, J. S. Kim, W. B. Jung, H. W. Yoo, J. Kim and H. T. Jung, *ACS Nano*, 2015, **9**, 9314–9321.
- 14 F. M. Enejekwu, Y. Zhang, C. I. Ezech, H. T. Zhao, M. X. Xu, E. Besley, M. W. George, N. A. Besley, H. N. Do and T. Wu, *Appl. Surf. Sci.*, 2021, **542**, 148556.
- 15 H. N. Kuang, Z. Y. He, M. Li, R. F. Huang, Y. Q. Zhang, X. M. Xu, L. Wang, Y. Chen and S. F. Zhao, *Chem. Eng. J.*, 2021, **417**, 127987.
- 16 Y. Gui, J. Shi, P. Yang, T. Li, C. Tang and L. Xu, *High Voltage*, 2020, **5**, 454–462.
- 17 L. Jiao, H. Y. Yan, Y. Wu, W. L. Gu, C. Z. Zhu, D. Du and Y. H. Lin, *Angew. Chem., Int. Ed.*, 2020, **59**, 2565–2576.
- 18 N. Aguilar, M. Atilhan and S. Aparicio, *Appl. Surf. Sci.*, 2020, **534**, 147611.
- 19 Y. D. Zhu, K. Zhao, J. L. Shi, X. Y. Ren, X. J. Zhao, Y. Shang, X. L. Xue, H. Z. Guo, X. M. Duan, H. He, Z. X. Guo and S. F. Li, *ACS Appl. Mater. Interfaces*, 2019, **11**, 32887–32894.
- 20 H.-Y. Su, X. Ma and K. Sun, *Appl. Surf. Sci.*, 2022, **597**, 153614.
- 21 F. L. Ling, W. D. Xia, L. Li, X. J. Zhou, X. Luo, Q. Z. Bu, J. C. Huang, X. Q. Liu, W. Kang and M. Zhou, *ACS Appl. Mater. Interfaces*, 2021, **13**, 17412–17419.
- 22 J. C. Yang, H. L. Yao, Y. D. Guo, B. W. Yang and J. L. Shi, *Angew. Chem., Int. Ed.*, 2022, **61**, e202200480.
- 23 S. R. Ali and M. M. De, *ACS Appl. Mater. Interfaces*, 2022, **2c11245**.
- 24 Y. Wang, K. Qi, S. S. Yu, G. R. Jia, Z. L. Cheng, L. R. Zheng, Q. Wu, Q. L. Bao, Q. Q. Wang, J. X. Zhao, X. Q. Cui and W. T. Zheng, *Nano-Micro Lett.*, 2019, **11**, 102.
- 25 D. W. Wang, Q. Li, C. Han, Z. C. Xing and X. R. Yang, *Appl. Catal., B*, 2019, **249**, 91–97.
- 26 D. L. Li, W. L. Li and J. P. Zhang, *Appl. Surf. Sci.*, 2019, **484**, 1297–1303.
- 27 T. H. Zhu, X. R. Gan, Z. H. Xiao, S. Dai, H. R. Xiao, S. J. Zhang, S. C. Dong, H. M. Zhao and P. F. Wang, *Surf. Interfaces*, 2021, **27**, 101538.
- 28 Z. D. Li, X. X. Yang, D. He, W. H. Hu, S. Younan, Z. J. Ke, M. Patrick, X. H. Xiao, J. Huang, H. J. Wu, X. Q. Pan and J. Gu, *ACS Catal.*, 2022, 7687–7695.
- 29 H. C. Huang, J. Wang, J. Li, Y. Zhao, X. X. Dong, J. Chen, G. Lu, Y. X. Bu and S. B. Cheng, *ACS Appl. Mater. Interfaces*, 2020, **12**, 19457–19466.
- 30 Y. Gao, Z. W. Cai, X. C. Wu, Z. L. Lv, P. Wu and C. X. Cai, *ACS Catal.*, 2018, **8**, 10364–10374.
- 31 K. Y. Chen, J. K. Deng, X. D. Ding, J. Sun, S. Yang and J. Z. Liu, *J. Am. Chem. Soc.*, 2018, **140**, 16206–16212.
- 32 S. D. Huang, C. Shang, P. L. Kang, X. J. Zhang and Z. P. Liu, *Wiley Interdiscip. Rev.: Comput. Mol. Sci.*, 2019, **9**, e1415.
- 33 T. Mueller, A. Hernandez and C. Wang, *J. Chem. Phys.*, 2020, **152**, 050902.
- 34 C. Shang and Z. P. Liu, *J. Chem. Theory Comput.*, 2013, **9**, 1838–1845.



- 35 S. Ma, C. Shang and Z.-P. Liu, *J. Chem. Phys.*, 2019, **151**, 050901.
- 36 J. Hafner, *J. Comput. Chem.*, 2008, **29**, 2044–2078.
- 37 J. P. Perdew, K. Burke and M. Ernzerhof, *Phys. Rev. Lett.*, 1996, **77**, 3865–3868.
- 38 G. Kresse and J. Furthmüller, *Comput. Mater. Sci.*, 1996, **6**, 15–50.
- 39 S. Grimme, J. Antony, S. Ehrlich and H. Krieg, *J. Chem. Phys.*, 2010, **132**, 154104.
- 40 W. H. Fu, X. Zhang, L. Q. Mei, R. Y. Zhou, W. Y. Yin, Q. Wang, Z. J. Gu and Y. L. Zhao, *ACS Nano*, 2020, **14**, 10001–10017.
- 41 J. N. Li, W. Q. Liu, X. C. Wu and X. F. Gao, *Biomaterials*, 2015, **48**, 37–44.
- 42 J. K. Nørskov, J. Rossmeisl, A. Logadottir, L. Lindqvist, J. R. Kitchin, T. Bligaard and H. Jonsson, *J. Phys. Chem. B*, 2004, **108**, 17886–17892.

